

Accurate and flexible neural-network interatomic potential for mixed materials: $\text{Ti}_x\text{Zr}_{1-x}\text{O}_2$ from bulk to clusters and nanoparticles

S. Rostami ^{1,*}, N. Seriani,¹ S. A. Ghasemi,² and R. Gebauer ¹

¹The Abdus Salam International Centre for Theoretical Physics, Strada Costiera 11, 34151 Trieste, Italy

²Department of Physics, Institute for Advanced Studies in Basic Sciences (IASBS), Zanjan 45137-66731, Iran



(Received 21 April 2021; accepted 16 June 2021; published 29 June 2021)

Many interesting systems, such as interfaces, surfaces, grain boundaries, and nanoparticles, contain so many atoms that quantum-mechanical atomistic simulations become inconvenient or outright impossible. It is therefore desirable to develop accurate and flexible general-purpose interatomic potentials to make it possible to explore the potential energy surface of such structures. In this work we generate a neural-network potential through charge equilibration technique (CENT) for $\text{Ti}_x\text{Zr}_{1-x}\text{O}_2$ with $0 \leq x \leq 1$. Optimized symmetry functions for multicomponent systems make it possible to train the potential on less than 10 000 diverse structures containing different cation ratios x , from pure TiO_2 to ZrO_2 , in free and periodic boundary conditions in the framework of density functional theory. The combination of the CENT potential with the symmetry functions generates a flexible and reliable method to reproduce the complexity of the energy landscape of these mixed materials with different boundary conditions at zero pressure. The reliability and transferability of the potential are verified by calculating some properties of bulk and slab configurations. Moreover, in order to investigate the performance of potential for different crystal phases and cluster configurations which are not included in our training data set, we performed a crystal structure search by minima hopping method. Beside reproducing known results in agreement with DFT calculations, we discovered novel crystal structures for bulk TiZr_3O_8 and TiZrO_4 , as well as for small clusters and ZrO_2 nanoparticles.

DOI: [10.1103/PhysRevMaterials.5.063605](https://doi.org/10.1103/PhysRevMaterials.5.063605)

I. INTRODUCTION

Atomistic simulations are recognized as an important tool to model and simulate material properties. Methods based on *ab initio* calculations like density functional theory (DFT) [1] can accurately predict properties in many cases, but are computationally expensive and therefore remain restricted to small cells with a few hundred atoms. This represents a severe limitation for the simulation of complex systems, like disordered structures, interfaces, and nanoparticles. On the other side, until recently, classical interatomic potentials struggled to reproduce DFT results in most cases. The field has changed through the introduction of artificial neural networks (ANN), which are very promising tools to generate reliable and fast interatomic potentials [2–6]. In recent years, ANN force fields have made tremendous progress, and are very good at mimicking DFT forces and energies at much lower computational cost.

The high-dimensional ANN method introduced by Behler and Parrinello is one of the most promising approaches for constructing the potential energy surface (PES) of materials and has been successfully employed in different applications [5]. In this model, a feed-forward ANN is built to interpolate the total energies as a function of environment dependent atomic descriptors through a learning process from a database obtained by electronic structure calculations. In most

ANN methods, the atomic descriptors are directly mapped to the atomic or total energies through the neural network; in this way, any physically interpretable connection is lost. In 2015, an alternative method based on a charge equilibration scheme was introduced to interpolate the electrostatic energy of systems with ionic interactions [7]. In this method, the charge equilibration via neural-network technique (CENT), only the environment-dependent electronegativity of atoms is interpolated by an ANN, and fed to an electrostatic model of the total energy. In this way, the total energy retains an expression which is interpretable with physical argument, and the black-box-like ANN interpolation is only used to connect the electronegativity of an atom to its environment. The reliability and transferability of CENT has been tested in different applications [8] and this model has been used to predict new crystal structures for ionic materials like ZnO [9], TiO_2 [10], and SrTiO_3 [11].

In the CENT potential, like in any ANN-based interatomic potential, the local atomic environment is described by environmental atomic descriptors, called symmetry functions. In the original form of the symmetry functions, introduced by Behler *et al.* [12,13], the number of symmetry functions increases quadratically with the number of atomic species. This becomes quickly problematic for multicomponent systems. As a result, the ANN potentials developed so far for multicomponent materials, while showing good transferability and accuracy, have been mostly applied to homogeneous systems and at fixed stoichiometry [11,13–15]. Only few studies show machine learning potentials at

*samare.rostami@gmail.com

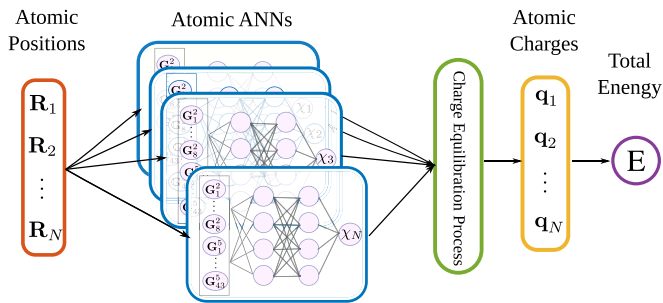


FIG. 1. A schematic representation of the CENT model.

varying stoichiometries, for amorphous Li_xSi [16], Mn_xGe_y [17], $\text{Li}_x\text{Mn}_2\text{O}_4$ [15], and $(\text{Co}_x\text{Mn}_{1-x})_3\text{O}_4$ compounds [18] just in specific lattice structures. The difficulties in generating ANN potentials for multicomponent materials stem from a large number of atomic descriptors, and also from the huge number of diverse structures needed as a reference database for the training process. Systems containing different species involve very diverse bonding between atoms and different atomic coordinations, resulting in a very complex energy landscape. Therefore, to generate a general potential for such a system, sampling of different parts of the complex energy surface is needed. As a result, it is common to use a large number of configurations for training and validation, even for binary compounds with fixed stoichiometry. Moreover, the root mean square error (RMSE) decreases linearly with the number of reference configurations [19]. So it would be useful if a method can suggest conditions which require many smaller databases to decrease computational costs

for generating the reference data and preparing the ANN potential.

Along this line of thought, Rostami *et al.* [20] introduced optimized symmetry functions with atom-dependent weights, which made the number of input nodes linear with respect to the number of atomic species. These descriptors overcome some of the problems of symmetry functions, and have been successfully applied to alkali-halide systems MX with six chemical species ($\text{M} = \{\text{Li}, \text{Na}, \text{K}\}$ and $\text{X} = \{\text{F}, \text{Cl}, \text{Br}\}$) [20]. Here we show that a combination of the CENT method with the symmetry functions by Rostami *et al.* constitutes a powerful tool to describe multicomponent materials, which is accurate and generalizes well. To demonstrate its capabilities, we apply it to materials of considerable scientific and technological interest. In this work we construct an ANN potential for $\text{Ti}_x\text{Zr}_{(1-x)}\text{O}_2$ with $0 \leq x \leq 1$ for free and periodic boundary conditions. The potential is trained on less than 10 000 DFT reference energies of diverse structures in different boundary conditions. Although our training data set is much smaller than in similar works, our developed ANN potential shows to be very reliable to reproduce different features of materials with a reasonable error with respect to the DFT reference results. We investigate its flexibility and transferability for a variety of complex systems like mixed bulk, interfaces, surfaces, clusters, and nanoparticles. Moreover, one of the important aspects of this potential is its ability to predict new material phases. Employing the minima hopping method (MHM) [21,22], we discover new structures for mixed bulks, small clusters, and ZrO_2 nanoparticles.

II. MATERIAL BACKGROUND

Titanium dioxide (TiO_2) and zirconium dioxide (ZrO_2) are important materials for a wide range of applications thanks

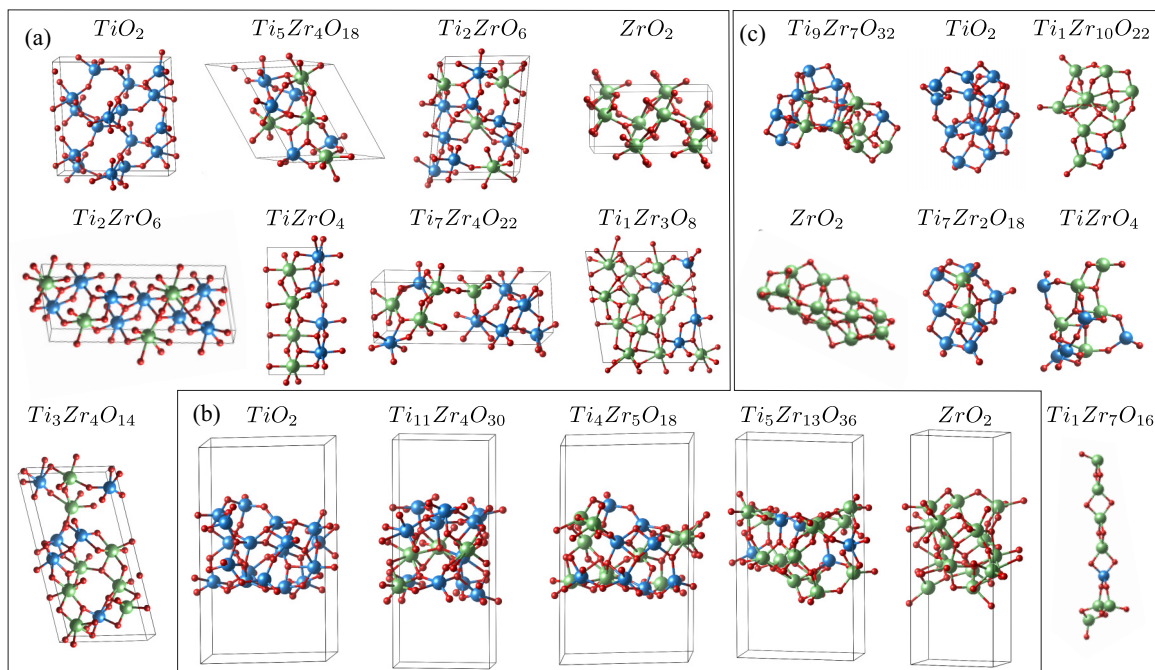


FIG. 2. Example of structures used for training and validation process in (a) bulk, (b) slab, and (c) free boundary conditions. In all figures, green, blue, and red balls indicate Zr, Ti, and O, respectively.

TABLE I. Number of configuration in the database and root mean square error on energy for different x in $\text{Ti}_x\text{Zr}_{(1-x)}\text{O}_2$.

Group	No. of structures		RMSE(E) (meV/atom)	
	Training	Validation	Training	Validation
$x = 0$	1444	267	6	7
$x = (0, 0.33]$	1868	285	7	8
$x = (0.33, 0.66)$	1799	302	8	8
$x = [0.66, 1)$	1636	266	7	8
$x = 1$	1723	270	6	6
Total	8470	1390	7	7

to their excellent physical and chemical properties. They are widely used, also at industrial level, either as pure materials, or, more often, with added impurities or in close contact with other compounds, which play significant roles in determining the performance of these materials.

These mixed compositions are crucial in many applications, like perovskite solar cells [23–25], dye-sensitized solar cells [26–28], and metal-insulator-metal (MIM) capacitors used in memory storage applications [29–31]. Instances of recent work comprise the investigation of the effect of Zr doping on stabilization and mechanical properties TiO_2 structures [32–34], enhancing current density of perovskite solar cells using $\text{TiO}_2/\text{ZrO}_2$ layers [23], and enhanced photocatalytic performance of TiO_2 by depositing ZrO_2 [35,36].

The degree of intermixing of the two compounds can vary strongly; as a consequence, much work has been devoted to explore this variety, to design and synthesize appropriate systems for the different applications, ranging from well-defined $\text{TiO}_2/\text{ZrO}_2$ interfaces [23–25,37], and coating one of these materials on substrates of the other one [26,32,38–40], to doping with small fraction of the cations [27,33,34,41,42] and completely mixed compositions [23,28–31,35,36,43–46]. Even fully mixed oxides display a variety of bonds, specially regarding Ti-O-Zr edges, and atomic coordinations, all of which affect chemical and electronic properties. Atomistic simulations can help to understand the underlying mechanism of formation of these structures and to design novel materials with useful properties.

ZrO_2 appears in three main polymorphs: a monoclinic structure, stable at low temperature, which converts to a tetragonal phase above 1170°C ; at 2370°C a cubic phase forms [47]. The well-known structure of pure TiO_2 at low temperature is anatase and a phase transition to rutile occurs in range $400\text{--}1200^\circ\text{C}$ [48]. More scarce information is available on the mixed crystals: one reported phase for $\text{Ti}_x\text{Zr}_{(1-x)}\text{O}_2$, ranging from $x = 0.43$ to 0.67 , is the $\alpha\text{-PbO}_2$ -type structure with space group $Pbcn$ where Ti and Zr are distributed randomly in the two cation sites [49–52]. Moreover, x-ray diffraction suggests the existence of crystallized anatase-type phases for $x < 0.5$ [41,53–57], and amorphous phases for other ratios. In addition to these structures, the crystallographic database of Materials Project reports another phase with space group $I42m$ for TiZrO_4 [58]. No other structures can be found in literature.

Also theoretical work on the mixed phases is much more scarce than on the well-studied TiO_2 and ZrO_2 structures. In different works, the band gap of some mixed configurations containing four different TiZrO_4 structures in $Pbcn$ space group symmetry, Zr doped TiO_2 , and ZrO_2 by Ti doping have been determined by means of DFT calculations [59–61]. Recently, Ismail and his co-workers simulated a bilayer of cubic ZrO_2 on a TiO_2 substrate [62]. Also the formation of mixed Zr-O-Ti bonds are briefly studied by simulation of the interface of two very thin slabs [63]. Clearly all the work published to date is far from providing a systematic view of the energy landscape of the mixed compositions. The high computational cost of such an investigation has been so far the limiting factor, and in the following we are going to show how CENT overcomes these limitations in a fast and accurate way.

III. METHOD

The CENT potential is a neural-network force field. In typical high-dimensional neural-networks models, the neural network accepts symmetry functions, which contain information on the atomic coordinates [12], as inputs, and evaluates directly the total energy as output. In this way, little physical information is encoded in the functional form of the energy. On the contrary, in CENT the neural network itself is not used to directly evaluate the energy, but to describe an atomic quantity, the electronegativity [7], which enters in the expression

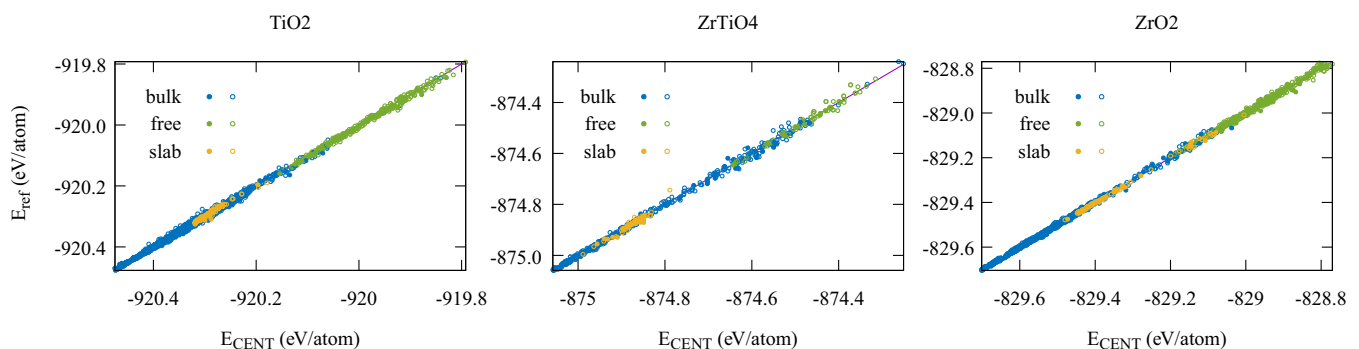


FIG. 3. Comparison of the DFT and CENT energies for $x = 1$, $x = 0.5$, $x = 1$ in $\text{Ti}_x\text{Zr}_{(1-x)}\text{O}_2$. Filled and empty circles indicate the validation and training data, respectively.

TABLE II. Formation energy and lattice information of seven different compositions obtained by CENT and DFT calculation: ZrO_2 in monoclinic (ZrO_{2_m}) and tetragonal (ZrO_{2_t}) phases, TiO_2 in anatase (TiO_{2_a}) and rutile (TiO_{2_r}) phases, two reported structures for $TiZrO_4$ ($TiZrO_{4_s1}$ and $TiZrO_{4_s2}$), and a novel configuration of $TiZrO_4$ in anatase crystal ($TiZrO_{4_at}$). All energies are printed in eV/atom and lattice constant are in Å.

Bulk (space group)		CENT	DFT	Error
ZrO_{2_m} ($P2_1/c$)	Energy	-829.745	-829.747	0.002
	a	5.190	5.187	0.06%
	b	5.235	5.238	0.05%
	c	5.367	5.379	0.23%
	α, γ	90	90	
	β	99.90	99.68	
ZrO_{2_t} ($P4_2/nmc$)	Energy	-829.708	-829.710	0.002
	a	3.616	3.619	0.08%
	b	3.616	3.619	0.08%
	c	5.300	5.281	0.37%
	α, β, γ	90	90	
	B	174.76	173.02	1%
$TiZrO_{4_at}$ ($P-1$)	Energy	-875.114	-875.118	0.004
	a	3.955	3.972	0.43%
	b	5.795	5.794	0.01%
	c	7.801	7.811	0.13%
	α	109.59	109.69	
	β	90.03	90.09	
$TiZrO_{4_s1}$ [58] ($P1$)	Energy	-875.093	-875.094	0.001
	a	4.818	4.822	0.09%
	b	5.624	5.651	0.46%
	c	10.155	10.149	0.01%
	α	91.0569	90.5687	
	β	91.7157	91.4902	
$TiZrO_{4_s2}$ [58] ($P2_12_12$)	Energy	-875.073	-875.076	0.003
	a	4.740	4.761	0.44%
	b	5.111	5.125	0.27%
	c	5.700	5.699	0.01%
	α, β, γ	90	90	
	B	189.77	184.18	3%
TiO_{2_a} ($I4_1/amd$)	Energy	-920.516	-920.518	0.002
	a	3.799	3.798	0.02%
	b	3.799	3.798	0.02%
	c	9.719	9.700	0.19%
	α, β, γ	90	90	
	B	189.36	187.58	1%
TiO_{2_r} ($P4_2/mnm$)	Energy	-920.483	-920.486	0.003
	a	4.634	4.642	0.18%
	b	4.634	4.642	0.18%
	c	2.962	2.963	0.05%
	α, β, γ	90	90	
	B	240.56	211.94	13%

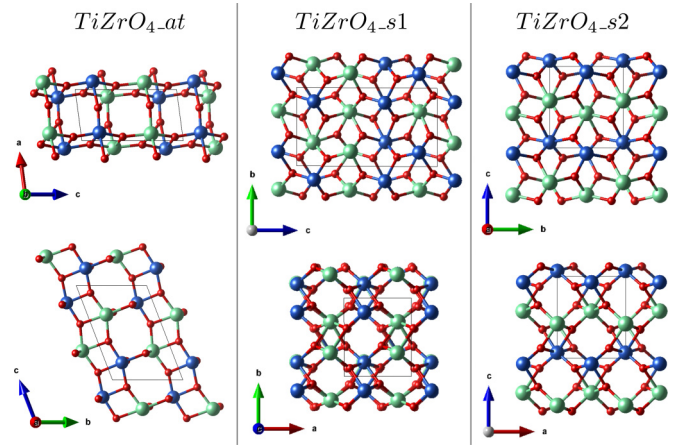


FIG. 4. $TiZrO_4$ structures.

of the total energy which has a clear physical interpretation. Indeed, the expression is based on the electronegativity equalization method (EEM) [64], which is a second order expansion of total energy with respect to atomic charges. As a consequence, the CENT energy is given by

$$U_{\text{tot}}(\{q_i\}) = \sum_{i=1}^N \left(E_i^0 + \chi_i q_i + \frac{1}{2} J_{ii} q_i^2 \right) + \frac{1}{2} \iint \frac{\rho(\mathbf{r})\rho(\mathbf{r}')}{|\mathbf{r} - \mathbf{r}'|} d\mathbf{r}d\mathbf{r}', \quad (1)$$

where E_i^0 are the energies of isolated atoms, q_i are the atomic charges, J_{ii} are the element-dependent atomic hardnesses, and χ_i is the environment dependent electronegativity of atom i . The charge density of the system $\rho(\mathbf{r})$ is a superposition of Gaussian charge densities on individual atoms which define by the following equation:

$$\rho_i(\mathbf{r}) = \frac{q_i}{\alpha_i^3 \pi^{3/2}} \exp\left(-\frac{|\mathbf{r} - \mathbf{r}_i|^2}{\alpha_i^2}\right), \quad (2)$$

where α_i is the Gaussian width of each atomic type. In the EEM model, the charges are allowed to flow among other atoms which lead to an equilibrium. Therefore, the atomic charges can be determined by minimizing the total energy of Eq. (1) with respect to q_i with a constraint that $\sum_i q_i = q_{\text{tot}}$:

$$\frac{\partial U_{\text{tot}}}{\partial q_i} = \chi_i + J_{ii} q_i + g_i = 0, \quad \forall i = 1, \dots, N, \quad (3)$$

where the gradient g_i is given by

$$g_i = \int \frac{\partial \rho(\mathbf{r})}{\partial q_i} d\mathbf{r} \int \frac{\rho(\mathbf{r}')}{|\mathbf{r} - \mathbf{r}'|} d\mathbf{r}'. \quad (4)$$

The CENT potential has improved the original EEM model through the assumption that the electronegativity explicitly depends on the atomic environments. The role of the ANN is to determine the functional relation of the electronegativity of an atom with the local environment given by the positions of the neighboring atoms. In this way, a physically interpretable form of the total energy is retained while harvesting the capabilities of the neural network. In Fig. 1, the whole structure of this feed-forward model is depicted. The atomic positions

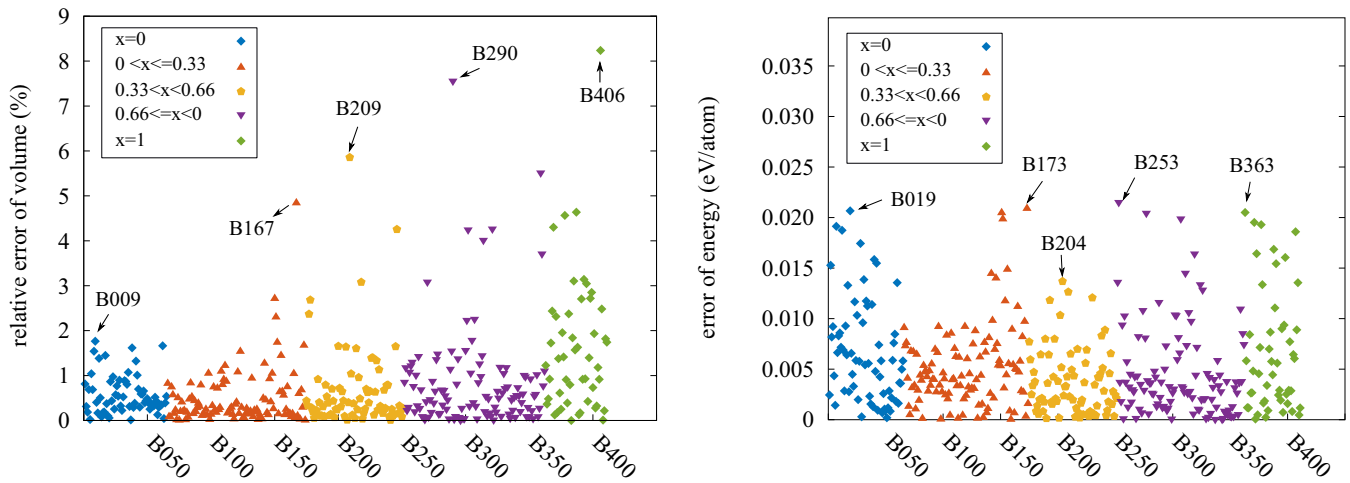


FIG. 5. Relative error on volumes and energies of our found structures with respect to PBE relaxed structures. Different colors in panels indicate the different ratio of x in $\text{Ti}_x\text{Zr}_{(1-x)}\text{O}_2$ formula.

are encoded into environment descriptors, the symmetry functions $\{G_i\}$ [12], which are the input layer of the ANN. To explore similarities of structures, we use optimized symmetry functions prepared for multicomponent systems which have a linear complexity with the number of different chemical species, as introduced in Ref. [20]. In these descriptors, the local environment of each atom is described by functions containing parameters and weights which depend on the chemical properties of atoms in its neighborhood. The radial G_i^2 and angular G_i^5 symmetry functions are given as

$$G_i^2 = \sum_j \omega_j e^{-\eta_j (R_{ij} - R_c)^2} f_c(R_{ij}), \quad (5)$$

$$G_i^5 = 2^{1-\zeta_i} \sum_{j,k} \omega_{ijk} (1 + \lambda_i \cos\theta_{ijk})^{\zeta_i} e^{-(\eta_j R_{ij}^2 + \eta_k R_{ik}^2)} \times f_c(R_{ij}) f_c(R_{ik}), \quad (6)$$

where ζ_i , λ_i , and η_i are the parameters which depend on the properties of atom i , while f_c is a cutoff function. Both atoms j and k are in the neighborhood of atom i in a cutoff radius. The weights ω_j and ω_{ijk} are governed by the electron affinities of the involved atoms, such as

$$\omega_j := \begin{cases} -1 & \text{if atom } j \text{ is a cation,} \\ +1 & \text{if atom } j \text{ is an anion,} \end{cases} \quad (7)$$

$$\omega_{ijk} := \omega_i(\omega_j + \omega_k) - 1.$$

In the present work, the ANN architecture contains two hidden layers and an output associated with the atomic electronegativity χ_i . The different layers of ANN are fully connected with weight parameters which have to be adjusted in order to find a correct energy landscape of the systems. In general, the expression of the atomic electronegativity with 51-8-8-1 architecture is given by

$$\chi_i = f_1^3 \left\{ b_1^3 + \sum_{l=1}^8 a_{l1}^{23} f_l^2 \left[b_l^2 + \sum_{k=1}^8 a_{kl}^{12} f_k^1 \left(b_k^1 + \sum_{j=1}^{51} a_{jk}^{01} G_i^{(j)} \right) \right] \right\},$$

where a_{jk}^{ij} and b_k^l are ANN weights which have to be optimized during the training process. A hyperbolic tangent activation

function f_k^l is used for all layers. Furthermore, we employ 51 symmetry functions $G_i^{(j)}$ including 8 radial and 43 angular functions. The goal of the training process is to minimize the cost function Γ with respect to ANN weights. In the current implementation of the CENT potential, the learning occurs through the reference energies E^{Ref} and the forces are used to evaluate the performance of the method for reproducing the derivative of the energy with respect to the space coordinate. Hence, the cost function is given by

$$\Gamma = \frac{1}{N_{\text{structure}}} \sum_{i=1}^{N_{\text{structure}}} \left(\frac{E_i^{\text{Ref}} - E_i^{\text{CENT}}}{N_{\text{atom}}} \right)^2,$$

where E^{CENT} is the CENT energy and $N_{\text{structure}}$ and N_{atom} are number of structures in the training database and number of atoms in each structure, respectively. For the fitting process, the global extended Kalman filter method [65,66] is employed.

Once χ_i are determined, in the charge equilibration process the atomic charges q_i can be obtained by minimizing the total energy in Eq. (1) with respect to q_i . The description of the CENT method and symmetry functions can be found in more detail in Refs. [7,20].

Summarizing, we use 51 symmetry functions (8 radial and 43 angular), and a neural network with 51-8-8-1 architecture. As a comparison, the original ANN by Behler *et al.* used 282 symmetry functions consisting of 3×8 radial and 6×43 angular symmetry functions to describe the atomic environments in the presence of different elements in a ternary system [12].

In order to predict new structures, we employ the minima hopping method (MHM) [21,22], which works with a sequence of short molecular dynamics simulations for escaping from local minima, followed by a geometry optimization. MHM ends up in local minima of the energy landscape and occasionally meets saddle points.

A. Computational details

To generate a database required for training and testing of ANN, we performed DFT calculations using the Perdew-

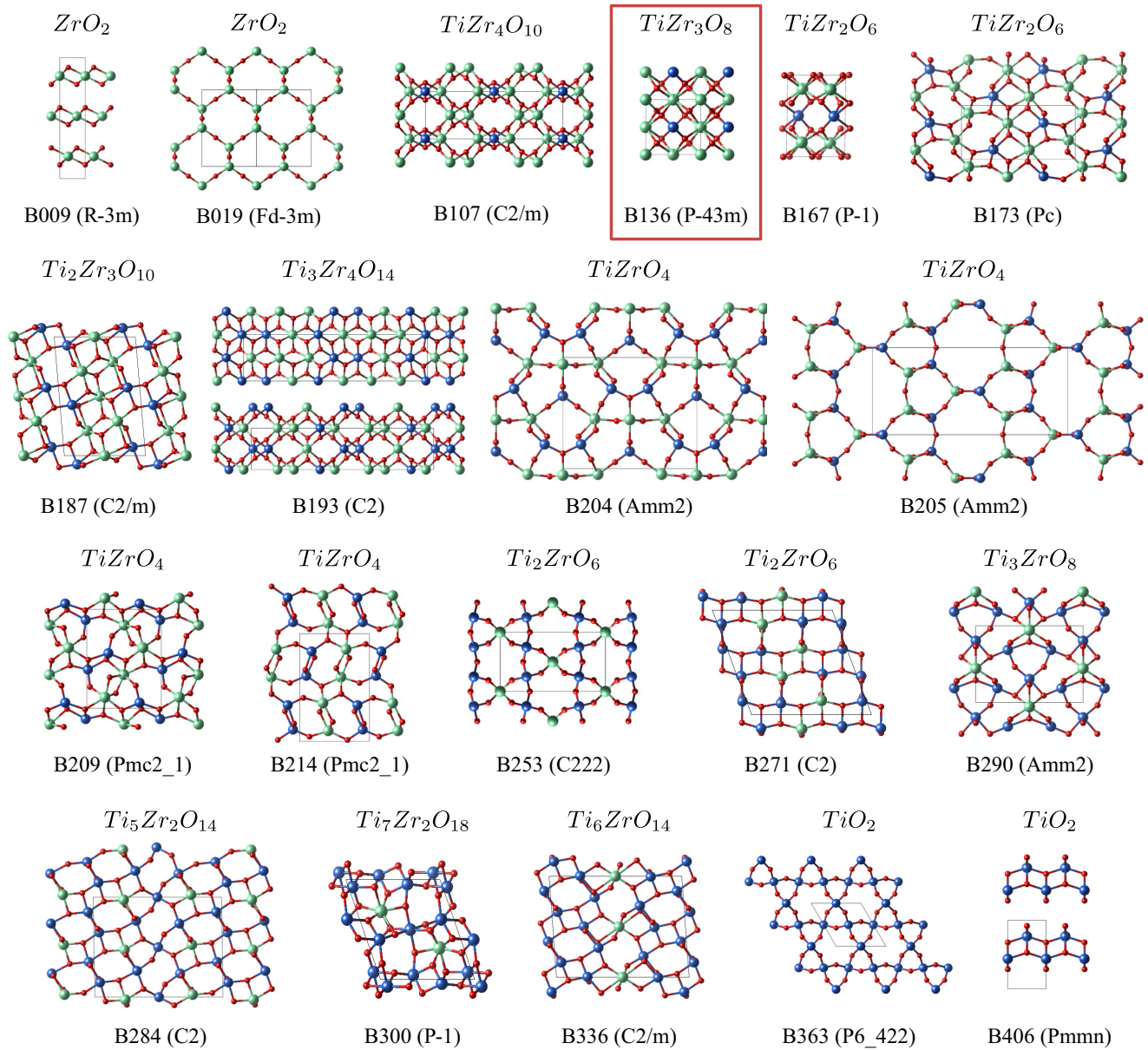


FIG. 6. New configurations of $Ti_xZr_{(1-x)}O_2$ predicted by the CENT potential. Below each structure is their index and in parentheses the space group in Hermann-Mauguin notation is listed.

Burke-Ernzerhof (PBE) [67] exchange correlation functional as implemented in the Quantum Espresso package [68]. Ultrasoft pseudopotentials [69] with a wave function energy cutoff of 50 Ry, a charge density cutoff of 200 Ry, and dense k -point meshes are chosen to converge the total energies to within 1 meV/atom. The k -point mesh is set by choosing the k -point density to be 0.04 \AA^{-3} . For simulating clusters and surfaces, in nonperiodic boundary condition directions a 12 \AA vacuum is employed to avoid the periodic effects. The ionic relaxations are converged to the threshold on forces to be 0.001 Ry/bohr . For all the calculations related to the ANN potential and crystal structure prediction approach, we employ a version of CENT and MHM method as implemented in the FLAME package [70] which is a library of atomistic modeling environments. At the end, the dynamical and thermal

properties are determined within the harmonic approximation through the Phonopy package [71].

B. Preparation of reference data and training the network

The CENT potential has to be trained by a set of reference structures with their energies and forces obtained in a framework of DFT calculations, analogously to the force-matching method used for conventional interatomic potentials [72,73]. To generate an appropriate and diverse database, we have performed different cycles of potential generation. The initial point was constructing a potential for pure ZrO_2 . First, we generated random configurations in bulk and cluster phases; moreover, starting from ZrO_2 phases reported in crystallographic databases, we produced structures where the atoms

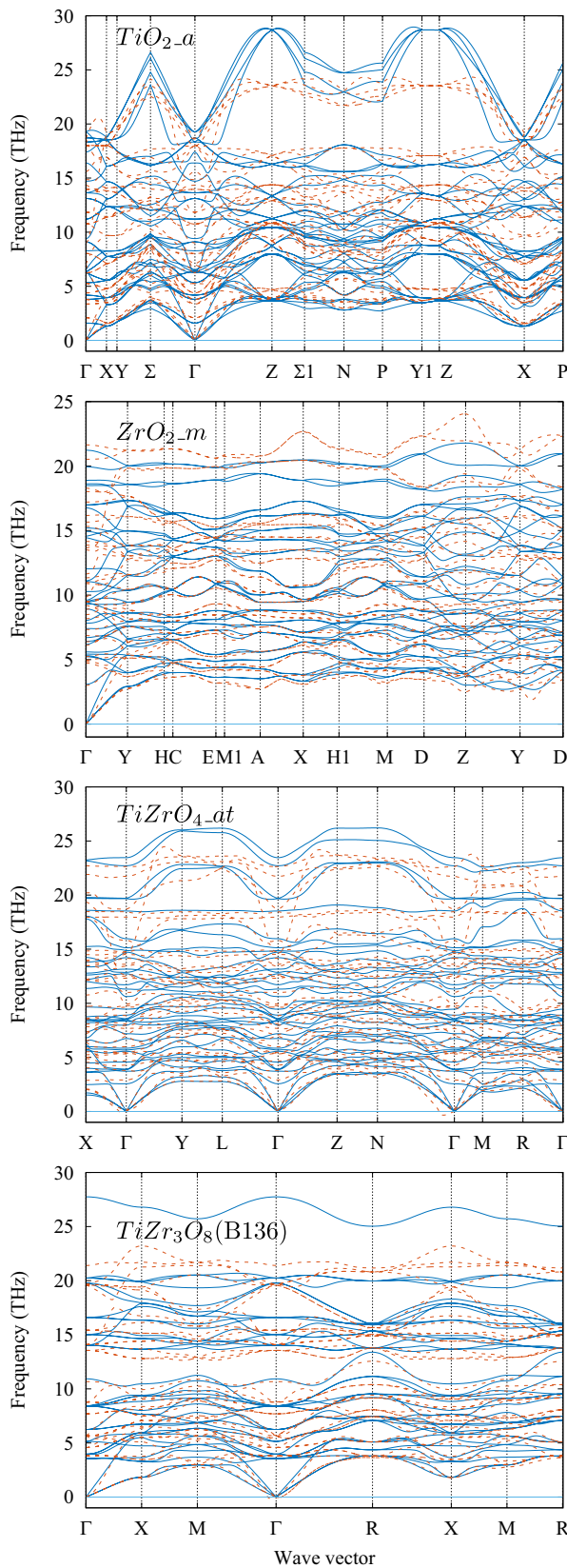


FIG. 7. Comparison of the phonon dispersion for four different compositions obtained by DFT (dashed lines) and CENT (solid lines) calculations: TiO_2 in anatase ($\text{TiO}_2\text{-a}$), ZrO_2 in monoclinic ($\text{ZrO}_2\text{-m}$), TiZrO_4 in anatase crystal ($\text{TiZrO}_4\text{-at}$), and TiZr_3O_8 (B136).

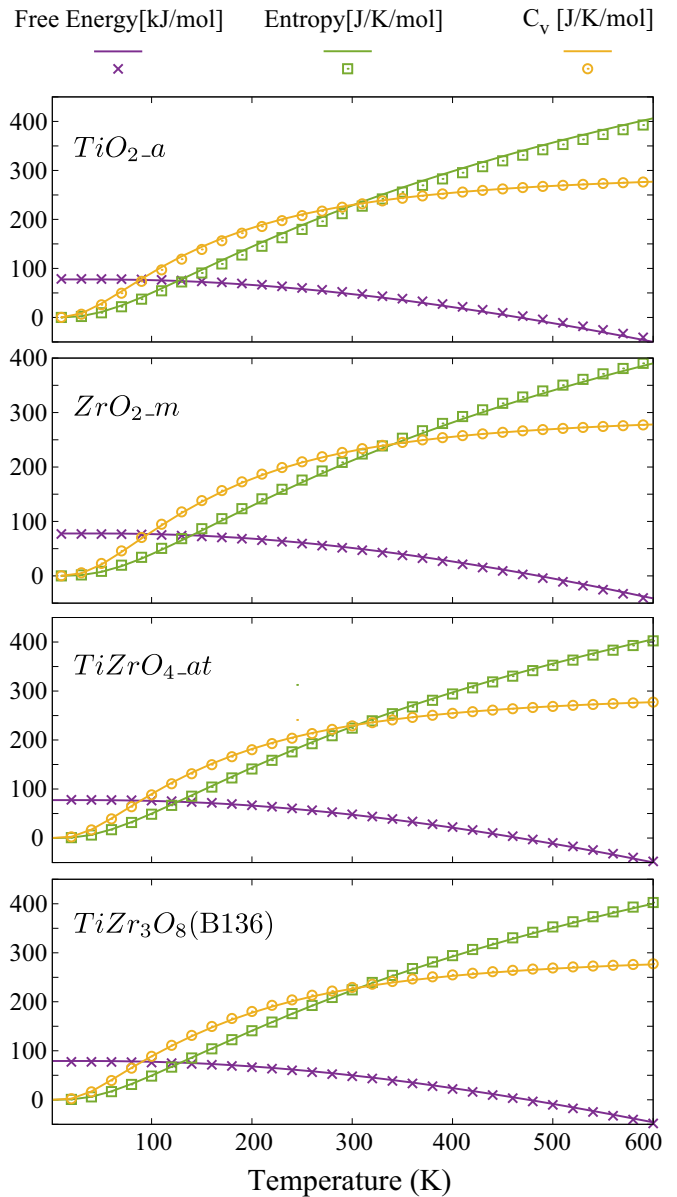


FIG. 8. Comparison of the thermal properties for four different compositions, using DFT (points) and CENT (solid lines) calculations: TiO_2 in anatase ($\text{TiO}_2\text{-a}$) phase, ZrO_2 in monoclinic ($\text{ZrO}_2\text{-m}$) phase, TiZrO_4 in anatase crystal ($\text{TiZrO}_4\text{-at}$), and TiZr_3O_8 (B136).

were slightly dislocated with random distance from their relaxed position. All these structures were used to train an ANN. Since our first generation of structures is not diverse enough and random configurations are not reasonable for the ZrO_2 energy landscape, the ANN potential could not work properly; still, we used it for short-time molecular dynamic simulations and geometry optimization with poor accuracy, to generate new structures so as to improve the reference data set of the following cycles. The new structures were selected either from snapshots of MD simulations, or from structural search via MHM, or by picking structures during the optimization path. This procedure is then repeated in subsequent cycles.

Once a potential for pure ZrO_2 was created, the diverse set of structures for ZrO_2 in bulk, slab, and clusters was used also

TABLE III. Surface energies and root mean square error of ionic displacements of surfaces for ZrO_2 , TiO_2 , and TiZrO_4 , obtained by DFT-PBE and CENT. The last columns show the atoms with largest displacement during geometry optimization from their bulk equilibrium positions.

Bulk	Face	Thickness (\AA)	Surface energy ($\text{meV}/\text{\AA}^2$)		Δr_{rms} ionic relaxation (\AA)			Displacement (\AA)	
			CENT	PBE	CENT	PBE		CENT	PBE
ZrO_2_{m}	(001)	21	77	79	0.206	0.196	O	-0.333	-0.288
ZrO_2_{m}	(010)	21	92	101	0.173	0.177	O	0.244	0.282
ZrO_2_{m}	(100)	20	91	88	0.091	0.099	O	0.080	0.112
ZrO_2_{t}	(001)	21	62	65	0.073	0.070	O	-0.180	-0.176
ZrO_2_{t}	(100)	19	60	56	0.988	1.038	Zr	-0.524	-0.561
ZrO_2_{t}	(101)	20	68	65	0.098	0.092	Zr	0.124	0.165
$\text{TiZrO}_4_{\text{al}}$	(001)	26	33	34	0.120	0.108	Ti	0.178	0.146
							Zr	-0.099	-0.132
$\text{TiZrO}_4_{\text{al}}$	(010)	30	61	65	0.040	0.058	Ti	0.133	0.109
$\text{TiZrO}_4_{\text{al}}$	(100)	23	37	35	0.161	0.192	Ti	0.339	0.376
							Ti	-0.317	-0.408
TiO_2_{a}	(001)	24	56	65	0.035	0.019	Ti	0.095	0.060
TiO_2_{a}	(100)	23	34	35	0.104	0.104	O	-0.173	-0.202
TiO_2_{a}	(110)	16	65	63	0.179	0.184	Ti	0.310	0.307

as a starting point for structures of the mixed oxides. Thus, instead of generating random structures for these oxides, we took the ZrO_2 structures and substituted a random number of Zr by Ti, taking care to cover the whole range of mixing ratios of $\text{ZrO}_2:\text{TiO}_2$. Since the bond lengths of Ti-O and Zr-O are different, swapping Zr with Ti will generate an unstable structure; for this reason, we selected 1000 structures and we let them undergo a few steps of structural optimization with DFT in order to create more reasonable reference data. Once we generated an ANN for mixed $\text{TiO}_2/\text{ZrO}_2$, for the next steps the geometry optimizations were performed by our CENT potential to achieve acceptable bond lengths. Analogous to the approach explained for producing the ZrO_2 potential, after eight cycles of improving the reference data set, we selected 9860 diverse structures to train our main CENT potential. Some of our configurations are shown in Fig. 2. Our final data set contains 7797 bulk and slab structures with sizes from 12 to 72 atoms in their cell and 2063 clusters consisting of 24 to 57 atoms. 86% of them were used for the training process and the remaining 14% for validation of the ANN potential.

The employed ANN architecture is 51-8-8-1, i.e., 51 symmetry functions (8 radial and 43 angular functions), and two hidden layers each with eight nodes, and the one-node output layer which produces the atomic electronegativity. The root mean squared error (RMSE) of the energy drops below 7 meV/atom within around 27 epochs. In Table I the distributions of error in training and validation set for different ratios x in $\text{Ti}_x\text{Zr}_{1-x}\text{O}_2$ are listed. As illustrated, the highest errors belong to combinations within $x = (0.33, 0.66)$ where the structures are more complex than in other groups. In Fig. 3 the CENT energies of TiO_2 , ZrO_2 , and TiZrO_4 are plotted against the DFT energies. In the panels, all data points for free, bulk, and slab boundary conditions are separated with different colors and the training and validation data are indicated via empty and filled circles, respectively. As illustrated in the figures, our data set continuously covers the range of energies

up to 0.7 eV above the lowest energy in each material group. The results show a good agreement between the reference and CENT energies.

Up to now we have shown that our CENT potential can reproduce energies of a given data set; now its flexibility and applicability should be examined for different structures, not included in the database. In the following sections we represent some structural and dynamical properties in bulk, slab, and free boundary conditions.

IV. RESULTS AND DISCUSSIONS

A. Lattice constants

First, using the CENT potential, we compute the lattice constant of the known structures of ZrO_2 , TiO_2 , and TiZrO_4 . Table II contains energy and lattice information obtained by PBE and CENT potentials for ZrO_2 in monoclinic (ZrO_2_{m}) and tetragonal (ZrO_2_{t}) phases, TiO_2 in anatase (TiO_2_{a}) and rutile (TiO_2_{r}) phases, and two reported structures for (TiZrO_4) with space group of $P1$ ($\text{TiZrO}_4_{\text{s1}}$) and $P2_12_1$ ($\text{TiZrO}_4_{\text{s1}}$) [49,50,58]. Both $\text{TiZrO}_4_{\text{s1}}$ and $\text{TiZrO}_4_{\text{s2}}$ have a similar α - PbO_2 -type structure in which Ti or Zr are substituted in cation lattice sites as shown in Fig. 4. We also add a novel phase for TiZrO_4 , which is discovered in our crystal structure search. This new configuration ($\text{TiZrO}_4_{\text{at}}$) has an anatase crystal, with a partial substitution of Ti through Zr, as depicted in Fig. 4. Even if these structures are present in the training database, still, they represent a small fraction of the structures used in the training, and therefore it is important to check that they are well described by the final potential. As illustrated in Table II, for these phases the relative error on lattice constant in comparison to PBE results is less than 1% and the absolute error on energies for pure and mixed components are less than 3 and 5 meV/atom, respectively. Our DFT-PBE calculation verifies that our new structure $\text{TiZrO}_4_{\text{at}}$ is energetically 20 meV/atom lower than the already reported phase

for TiZrO_4 . Thus, already at this level, the potential shows its usefulness by predicting a novel, hitherto unseen crystal structure for TiZrO_4 .

To investigate the performance of CENT potential for mechanical properties, we calculated the bulk modulus of these seven compounds by fitting volume-energy data to the Birch-Murnaghan equation of state. The values of the bulk modulus B are listed in Table II and their corresponding energy vs volume plots are presented in the Supplemental Material (SM) [74]. Except the TiO_2 _r structure, the error on the bulk modulus is less than 1% for our pure material and less than 3% for our mixed systems. The energy/volume plots show that the CENT results for all of our material in a compressed situation is well fitted to the PBE and the error on bulk modulus is mostly due to the error for energies in the expanding state. So it indicates that our CENT potential works better at higher pressures.

B. Predicting new phases

An appropriate potential should reproduce different parts of the energy landscape apart from the vicinity of data points involved in the training process. Therefore, to investigate the flexibility of potential, we explored the potential energy surfaces $\text{Ti}_x\text{Zr}_{(1-x)}\text{O}_2$ with ($0 < x < 1$) by applying a crystal structure method to discover new phases.

We performed MHM for different ratios of Ti and Zr in configurations consisting of 9 to 30 atoms in fully periodic boundary conditions. Due to the diversity caused by using different ratios of Zr and Ti atoms, we generate 60 categories for all possible components from 9 to 30 atoms. In fact, substituting Ti or Zr in a cell containing n formula unit of MO_2 ($M = \text{Ti, Zr}$) we have $n + 1$ possible stoichiometric compounds. For each category we carry out about ten different MHM searches, with different initial configurations and with short-time simulations. In this way we discovered more than 50 000 new different structures. It is a sign of the capability of the methods that, even though only short-time simulations were employed, we were able to find thousands of different configurations. Our training and validation reference data contains 7797 periodic phases, which are different from one another, but do not represent different phases, since, for example, many of them are snapshots from the same MD simulation. As a consequence, we can conclude that more than 90% of our found structures are not included in the training process and are totally new and untrained parts of the energy landscape. For this study we do not mean to focus our attention on searching and finding all global minima and stable structures of these mixed materials. This number of new phases is sufficient for us to explain that our potential is flexible enough to produce new forms of these components.

As a further check, we took 460 of the novel structures and optimized again by DFT-PBE. After full optimization with DFT-PBE, 411 structures, i.e., 90% of the considered structures, stayed in the same shape with a small deformation in the lattice constants and atomic positions.

In Fig. 5 we plot the relative error of volume error on energy and volume of these phases relaxed by the CENT potential with respect to the PBE relaxed ones. In the figures we separate the difference cation ratio by colors and

indicate the structures with the largest error in each panel. The related configurations together with some of our found phases are depicted in Fig. 6. As shown in this figure, our potential generates very diverse and complex structures with different densities and even layered structures. As illustrated in Fig. 6, the largest error in the volume for pure material belongs to the layered structures B009 and B406. In the mixed phases, the largest errors on energy and volume are associated with complicated phases. For these relaxed structures, the root mean square error of the CENT energy with respect to PBE is 7 meV/atom, in the range of error in our training and validation process. In total, the results show that the relative error on volume of 92% of structures is less than 2% and the energy difference of 87% of our found phases is less than 10 meV/atom.

C. Dynamical properties

For the next step of assessing the accuracy of CENT potential, we evaluate the phonon dispersions. For this aim we perform Phonopy package [71] which is based on the finite-displacement method. Since for mixed structures the phonon calculation needs a large number of displacements, and the computations on supercells are computationally expensive, we just computed it for a few structures and found a good agreement between PBE and CENT results. In Fig. 7 the phonon dispersion for our four important structures are illustrated. We choose the global minima of pure materials ZrO_2 _m and TiO_2 _a, and our found global state for equally mixed component TiZrO_4 _at. We also pick a novel structure for TiZr_3O_8 with a high symmetry, with space group 215 ($P - 43m$), which is depicted as B136 in Fig. 6. For these structures we generate $3 \times 3 \times 3$ supercells for ZrO_2 _m and TiZr_3O_8 , $4 \times 4 \times 2$ supercells for TiO_2 _a, and $4 \times 3 \times 2$ supercells for TiZrO_4 _at. As we show in Fig. 7, the PBE frequencies (dashed lines) are in good agreement with the CENT results (solid lines), specially for low frequencies and acoustic modes. Furthermore, all frequencies of TiZrO_4 _at and TiZr_3O_8 are positive, showing that they are dynamically stable at zero temperature.

From the phonon frequencies, thermal properties have been calculated in the harmonic approximation. Free energy F , entropy S , and heat capacity at constant volume C_V are expressed as

$$F = \frac{1}{2} \sum_{q,s} \hbar\omega(q,s) + k_B T \sum_{q,s} \ln\{1 - \exp[-\hbar\omega(q,s)/k_B T]\},$$

$$S = -k_B \sum_{q,s} \ln\{1 - \exp[-\hbar\omega(q,s)/k_B T]\}$$

$$- \frac{1}{T} \sum_{q,s} \frac{\hbar\omega(q,s)}{\exp[\hbar\omega(q,s)/k_B T] - 1},$$

$$C_V = \sum_{q,s} k_B \left[\frac{\hbar\omega(q,s)}{k_B T} \right]^2 \frac{\exp[\hbar\omega(q,s)/k_B T]}{\{\exp[\hbar\omega(q,s)/k_B T] - 1\}^2},$$

where $\omega(q,s)$ is frequency of different modes, and T and k_B are temperature and Boltzmann constant, respectively. The thermal properties for mentioned structures are plotted in

Fig. 8. The results show a good match between thermal properties obtained by CENT and PBE.

D. Surfaces

We investigated the accuracy of the CENT potential also for surface properties, by considering low-index surfaces of stable TiO_2 , ZrO_2 , and TiZrO_4 -al phases. The surface energy for the relaxed surfaces were computed as

$$E = \frac{1}{2A}(E^s - nE^b),$$

where E^s and E^b are the energies of the relaxed surface and the energy per formula unit of the perfect bulk, respectively. The factor 2 in the denominator comes from the fact that the slab geometry includes two equivalent surfaces with area A . As an indicator of geometric changes of the surface, we calculated the root mean square of displacement of the atoms with respect to their bulk positions. Low-index surfaces were calculated for the anatase phase of TiO_2 and for the tetragonal and monoclinic phases of ZrO_2 . We considered also the (001), (010), and (100) surfaces of the novel TiZrO_4 -at phase. Table III contains the formation energy of different surfaces and root mean square of atomic displacements. As the movement of atoms close to the surface are different from the center of slabs, we also listed the largest individual displacements of each structure. The CENT potential can reproduce surface geometry and energies from DFT. The largest errors belong to the (101) facet of ZrO_2 -m and to the (001) facet of TiO_2 -a, both being $9 \text{ meV}/\text{\AA}^2$. In both PBE and CENT, ZrO_2 -t (100) is not stable; relaxation induces a deformation of the whole slab and the appearance of a different phase.

E. Cluster

We tested the CENT potential also for the energy landscape of clusters and nanoparticles. We applied MHM to explore the energy landscape of the limiting cases $(\text{Zr}_2\text{O}_4)_n$, $(\text{Ti}_2\text{O}_4)_n$, and $(\text{TiZrO}_4)_n$ for $n \leq 6$. We expect the potential to be equally accurate also at intermediate stoichiometries, but we limited ourselves to these stoichiometries to limit the computational cost.

The difficulty of finding new structures is that for every n , there are $n + 1$ different combinations in the form of $(\text{TiO}_2)_m(\text{ZrO}_2)_{n-m}$ with $0 \leq m \leq n$, and for each of them one should perform several MHM jobs separately to be sure that the entire PES is fully explored. At last, in consideration of the errors of the CENT potential, all structures with energies 20 meV/atoms above the global minimum were optimized gain by DFT to confirm the correct energetic ordering. Moreover, for each combination, we need diverse initial configurations for MHM runs. Indeed, for our multicomponent configuration, swapping a Ti with Zr will generate a new configuration and MHM needs so many steps to find and cross the appropriate barriers through the path of exchanging these elements. To avoid very long MHM runs, we increase the performance by using different substitutions of Ti and Zr in initial structures.

In recent times, some studies have been done to inquire about the global minimum of ultrasmall clusters of ZrO_2 and TiO_2 [75–85]. Structural search for $(\text{Zr}_2\text{O}_4)_n$, $(\text{Ti}_2\text{O}_4)_n$ with our potential predicted all global minima for $n \leq 5$, in agree-

ment with the findings of Ref. [84]. Moreover, for $(\text{Ti}_2\text{O}_4)_6$ and $(\text{Zr}_2\text{O}_4)_6$ we found structures which have a lower energy than the global minima reported in the literature for these clusters. For both $(\text{Ti}_2\text{O}_4)_6$ and $(\text{Zr}_2\text{O}_4)_6$, our new lowest energy configurations have energies about 5 meV/atom lower than the global minimum listed in Ref. [84]. All found structures by ANN are again optimized by DFT and the energies and configurations are reported. The atomic positions of all structures are listed in the SM [74]. Clusters of ZrO_2 and TiO_2 display a large variety of structural features, but, still, the CENT potential can deal with them reasonably well. We would like to note that the smallest cluster we used in our training data set has 24 atoms, and no structures of this small size were included in the training.

The low-energy clusters of $(\text{TiZrO}_4)_n$ resemble those of either TiO_2 or ZrO_2 , with swapped cations. For $n = 1, 2$, and 5, the clusters of both TiO_2 and ZrO_2 are built with the same construction and as well we can therefore also find similar clusters for $(\text{TiZrO}_4)_n$. The predicated global state for $n = 3$ and $n = 4, 6$ are inherited from TiO_2 and ZrO_2 clusters, respectively. As shown in Fig. 9, every substitution of elements can change the energies and the position of elements in configurations are significantly important. Here we present just a few representative configurations as examples, however our structural search discovered several identical configurations differing by permutation of cations. MHM predicts a variety of possible configurations; some of the high-symmetry clusters are illustrated in Fig. 9.

F. Nanoparticles

To investigate the performance of our potential for nanoparticles (NPs), we generated some well-known stable structures of TiO_2 and ZrO_2 and optimized them with the CENT potential. We generated our nanoparticles from tetragonal ZrO_2 phase and anatase TiO_2 by cutting $\{101\}$ surfaces, which are the most stable surfaces for these materials [86–89]. Consequently, stoichiometric NPs for TiO_2 and nonstoichiometric NPs for ZrO_{2-x} can be shaped. The properties of these NPs have been investigated by DFT in other studies [90–97] which we have used to benchmark our results.

The TiO_2 NPs have an octahedral shape; the size along axes perpendicular to its mirror plane is almost twice of other axes and is terminated in a single O on the top. The optimized NPs via CENT are in good agreement with PBE results, with very slight expansion in the top octahedrals along the longest axes (the final structures are presented in the SM [74]). The $\{101\}$ truncation of tetragonal ZrO_2 can generate nonstoichiometric ZrO_{2-x} structures which can be made stoichiometric by removing some Zr atoms from corners of octahedrals. The nonstoichiometric structures are particularly interesting, because these configurations are not present in the training database and therefore provide a stronger test of transferability for our CENT potential. $\text{Zr}_{19}\text{O}_{32}$, $\text{Zr}_{44}\text{O}_{80}$, $\text{Zr}_{85}\text{O}_{160}$, and $\text{Zr}_{146}\text{O}_{280}$ have been considered. By relaxation of $\text{Zr}_{44}\text{O}_{80}$, $\text{Zr}_{85}\text{O}_{160}$, and $\text{Zr}_{146}\text{O}_{280}$, novel structures are obtained, which are not reported in the literature [90–94]. In Fig. 10 these novel configurations are illustrated. The novel structure of $\text{Zr}_{44}\text{O}_{80}$ [Fig. 10(c)] differs from the one reported in the literature [Fig. 10(b)] by the displacement of atoms on the four

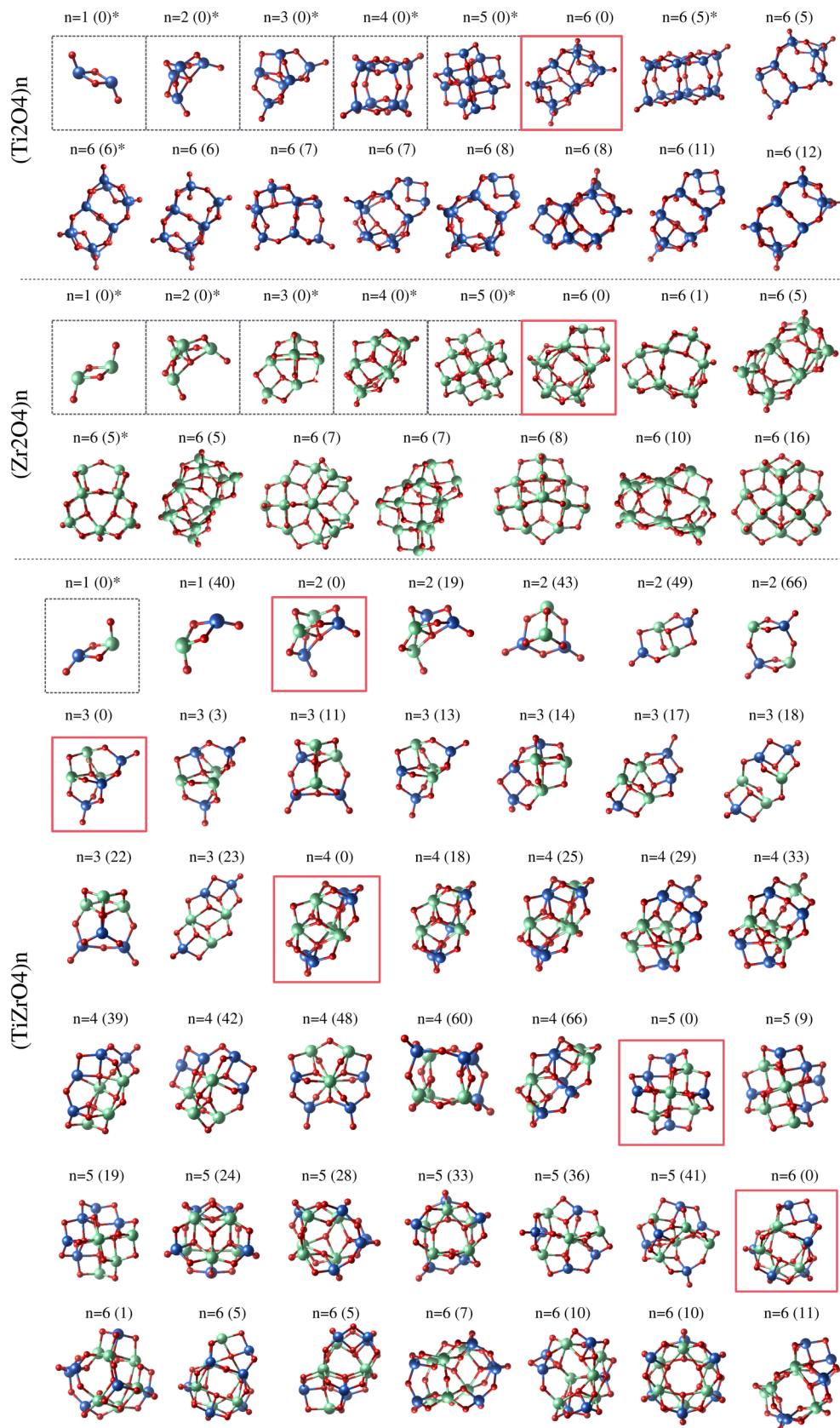


FIG. 9. Different clusters for (Ti₂O₄)_n, (Zr₂O₄)_n, and (TiZrO₄)_n for n = 1–6. In all structures, green, blue, and red spheres belong to Zr, Ti, and O elements, respectively. The squares indicate the global state of each size and the red and dashed ones belong to our new found clusters and already reported ones, respectively. The number in parentheses shows the relative energy with respect to the global minimum in each size in meV/atom. Stars illustrate the already reported clusters.

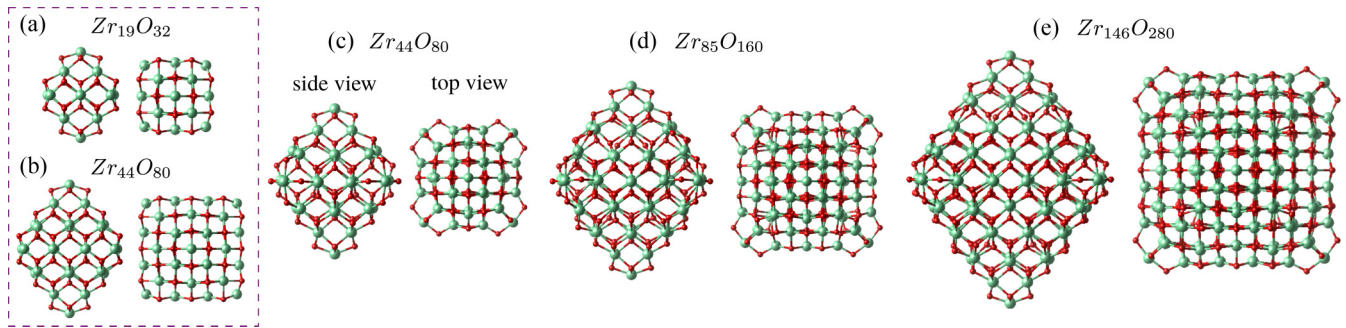


FIG. 10. The nanoparticles of ZrO_{2-x} . All structures are presented in top and side views. Two structures (a) and (b) in the dashed box are already reported in other works and the rest are our predicted configurations.

corners of the octahedra. DFT-PBE relaxation confirms that all these structures are local minima; the new configurations $\text{Zr}_{44}\text{O}_{80}$ and $\text{Zr}_{85}\text{O}_{160}$ lie 22 and 30 meV/atom, respectively, lower in energy than the known ones. The structures are reported in the SM [74].

Here we just present optimized structures starting from a clean cut of bulks and the results show that CENT potential predicts structures which are energetically more favorable than the already reported ones. The facets of octahedra are chosen from the stable surfaces of ZrO_2 and due to starting from symmetric structures, the DFT method gets stuck in a local minimum and could not find other basins with lower energies. However, small deformations of the original configuration and breaking the symmetries on edges may lead to new local minima with lower energy. Since DFT calculations for systems with many atoms are computationally expensive, it does not allow us to explore many such low-symmetry constructions; as a consequence, the ANN method plays an important role to predict novel structures.

V. CONCLUSIONS

We generated a CENT interatomic potential for the mixed oxides $\text{Ti}_x\text{Zr}_{(1-x)}\text{O}_2$ with $0 \leq x \leq 1$ which can reproduce the energy landscape of these materials in all boundary conditions. The database for the training and validation of the potential contains only 9860 structures in different boundary conditions and mixing conditions; this is a smaller data set than those used in the literature, even for pure materials. The key factor enabling the use of such a small training data set

is the employment of symmetry functions which have been recently developed for multicomponent systems [20]. The potential has been validated by comparing bulk and surface properties with the corresponding DFT-PBE results.

To further test the capabilities of the CENT potential, we applied it in the search of novel crystal structures, in combination with the minima hopping method. The potential successfully predicted more than 50 000 structures which can be either a local minimum or a saddle point. Out of these, we selected 400 low-energy structures and performed a direct comparison with DFT-PBE calculations; the error on the energy is in the same range as the error in the training process, further testifying excellent transferability of the potential. As a result, we found a new stable phase for TiZr_3O_8 (B136) and also a novel anatase type structure for TiZrO_4 which is energetically lower in energy than other reported phases in crystallography databases. Moreover, in structural prediction for small clusters, we found new global minima for $(\text{ZrO}_2)_{12}$ and $(\text{TiO}_2)_{12}$ and also global state and novel structures for $(\text{TiZrO}_4)_n$ for $n = 2-6$. Finally, we found that structural modifications of some ZrO_2 nanoparticles lead to their further stabilization.

In conclusion, we have developed a CENT interatomic potential for oxides of titanium and zirconium that reproduces the energy landscape in a wide range of situations, such as bulk mixed oxides, interfaces, surfaces, clusters, and nanoparticles, for any ratio of TiO_2 and ZrO_2 and even for complex structures involving unusual Zr-O-Ti bonds. This potential creates unprecedented possibilities to simulate complex interfaces and nanostructures of $\text{Ti}_x\text{Zr}_{(1-x)}\text{O}_2$ at the atomistic level.

- [1] W. Kohn and L. J. Sham, *Phys. Rev.* **140**, A1133 (1965).
- [2] S. Lorenz, A. Gross, and M. Scheffler, *Chem. Phys. Lett.* **395**, 210 (2004).
- [3] M. Rupp, A. Tkatchenko, K.-R. Müller, and O. A. von Lilienfeld, *Phys. Rev. Lett.* **108**, 058301 (2012).
- [4] A. P. Bartók, M. C. Payne, R. Kondor, and G. Csányi, *Phys. Rev. Lett.* **104**, 136403 (2010).
- [5] J. Behler and M. Parrinello, *Phys. Rev. Lett.* **98**, 146401 (2007).
- [6] E. Alpaydin, *Introduction to Machine Learning, Second Edition (Adaptive Computation and Machine Learning)* (The MIT Press, Cambridge, 2010).
- [7] S. A. Ghasemi, A. Hofstetter, S. Saha, and S. Goedecker, *Phys. Rev. B* **92**, 045131 (2015).
- [8] S. Faraji, S. A. Ghasemi, S. Rostami, R. Rasoulkhani, B. Schaefer, S. Goedecker, and M. Amsler, *Phys. Rev. B* **95**, 104105 (2017).
- [9] R. Rasoulkhani, H. Tahmasbi, S. A. Ghasemi, S. Faraji, S. Rostami, and M. Amsler, *Phys. Rev. B* **96**, 064108 (2017).
- [10] H. A. Eivari, S. A. Ghasemi, H. Tahmasbi, S. Rostami, S. Faraji, R. Rasoulkhani, S. Goedecker, and M. Amsler, *Chem. Mater.* **29**, 8594 (2017).

- [11] E. R. Khajepasha, S. Goedecker, and S. A. Ghasemi, *J. Comput. Chem.* **42**, 699 (2021).
- [12] J. Behler, *J. Chem. Phys.* **134**, 074106 (2011).
- [13] N. Artrith, B. Hiller, and J. Behler, *Phys. Status Solidi B* **250**, 1191 (2013).
- [14] W. Li, Y. Ando, E. Minamitani, and S. Watanabe, *J. Chem. Phys.* **147**, 214106 (2017).
- [15] M. Eckhoff, F. Schönewald, M. Risch, C. A. Volkert, P. E. Blöchl, and J. Behler, *Phys. Rev. B* **102**, 174102 (2020).
- [16] N. Artrith, A. Urban, and G. Ceder, *J. Chem. Phys.* **148**, 241711 (2018).
- [17] C. Mangold, S. Chen, G. Barbalinardo, J. Behler, P. Pochet, K. Termentzidis, Y. Han, L. Chaput, D. Lacroix, and D. Donadio, *J. Appl. Phys.* **127**, 244901 (2020).
- [18] S. K. Wallace, A. S. Bochkarev, A. van Roekeghem, J. Carrasco, A. Shapeev, and N. Mingo, *Phys. Rev. Mater.* **5**, 035402 (2021).
- [19] S. ichi Amari and N. Murata, *Neural Comput.* **5**, 140 (1993).
- [20] S. Rostami, M. Amsler, and S. A. Ghasemi, *J. Chem. Phys.* **149**, 124106 (2018).
- [21] S. Goedecker, *J. Chem. Phys.* **120**, 9911 (2004).
- [22] M. Amsler and S. Goedecker, *J. Chem. Phys.* **133**, 224104 (2010).
- [23] M. Che, L. Zhu, Y. Zhao, D. Yao, X. Gu, J. Song, and Y. Qiang, *Mater. Sci. Semicond. Process.* **56**, 29 (2016).
- [24] M. A. M. Escobar, S. Pathak, J. Liu, H. J. Snaith, and F. Jaramillo, *ACS Appl. Mater. Interfaces* **9**, 2342 (2017).
- [25] A. Priyadarshi, A. Bashir, J. T. Gunawan, L. J. Haur, A. Bruno, Z. Akhter, N. Mathews, and S. G. Mhaisalkar, *Energy Technol.* **5**, 1866 (2017).
- [26] D. B. Menzies, R. Cervini, Y.-B. Cheng, G. P. Simon, and L. Spiccia, *J. Sol-Gel Sci. Technol.* **32**, 363 (2004).
- [27] I. M. Mohamed, V.-D. Dao, N. A. Barakat, A. S. Yasin, A. Yousef, and H.-S. Choi, *J. Colloid Interface Sci.* **476**, 9 (2016).
- [28] A. Kitiyanan, S. Ngamsinlapasathian, S. Pavasupree, and S. Yoshikawa, *J. Solid State Chem.* **178**, 1044 (2005).
- [29] S. Lin, K. Chiang, A. Chin, and F. Yeh, *IEEE Electron Device Lett.* **30**, 715 (2009).
- [30] R. Padmanabhan, S. Mohan, Y. Morozumi, S. Kaushal, and N. Bhat, *IEEE Trans. Electron Devices* **63**, 3928 (2016).
- [31] Y.-S. Shen, K.-Y. Chen, P.-C. Chen, T.-C. Chen, and Y.-H. Wu, *Sci. Rep.* **7**, 43659 (2017).
- [32] Y. Gnatyuk, N. Smirnova, O. Korduban, and A. Eremenko, *Surf. Interface Anal.* **42**, 1276 (2010).
- [33] E. Holbig, L. Dubrovinsky, G. Steinle-Neumann, V. Prakapenka, and V. Swamy, *Z. Naturforsch. Teil B* **61**, 1577 (2006).
- [34] E. S. Holbig, Ph.D. thesis, Bayreuth, 2008.
- [35] X. Fu, L. A. Clark, Q. Yang, and M. A. Anderson, *Environ. Sci. Tech.* **30**, 647 (1996).
- [36] X. Wang, R. L. Patel, and X. Liang, *RSC Adv.* **8**, 25829 (2018).
- [37] K. P. Biju and M. K. Jain, *Sens. Actuators B* **128**, 407 (2008).
- [38] F. Li, Y. Jiao, J. Liu, Q. Li, C. Guo, C. Tian, and B. Jiang, *J. Colloid Interface Sci.* **561**, 568 (2020).
- [39] T. Ivanova, A. Harizanova, T. Koutzarova, N. Krins, and B. Vertruyen, *Mater. Sci. Eng. B* **165**, 212 (2009).
- [40] B.-T. Lee, J.-K. Han, A. K. Gain, K.-H. Lee, and F. Saito, *Mater. Lett.* **60**, 2101 (2006).
- [41] Y. Gnatyuk, N. Smirnova, A. Eremenko, and V. Ilyin, *Adsorpt. Sci. Technol.* **23**, 497 (2005).
- [42] A. M. Saleem, S. Gnanasaravanan, D. Saravanakkumar, S. Rajasekar, A. Ayeshamariam, and M. Jayachandran, *Mater. Today: Proc.* **36**, 408 (2021).
- [43] H. Zou and Y. Lin, *Appl. Catal. A: General* **265**, 35 (2004).
- [44] S. Anisah, M. Kanezashi, H. Nagasawa, and T. Tsuru, *J. Sol-Gel Sci. Technol.* **92**, 12 (2019).
- [45] V. S. Anitha, S. S. Lekshmy, and K. Joy, *J. Mater. Sci.: Mater. Electron.* **28**, 10541 (2017).
- [46] M. D. Hernández-Alonso, J. M. Coronado, B. Bachiller-Baeza, M. Fernández-García, and J. Soria, *Chem. Mater.* **19**, 4283 (2007).
- [47] M. H. Bocanegra-Bernal and S. D. de la Torre, *J. Mater. Sci.* **37**, 4947 (2002).
- [48] D. A. H. Hanaor and C. C. Sorrell, *J. Mater. Sci.* **46**, 855 (2010).
- [49] P. Bordet, A. McHale, A. Santoro, and R. Roth, *J. Solid State Chem.* **64**, 30 (1986).
- [50] U. Troitzsch, A. G. Christy, and D. J. Ellis, *Phys. Chem. Miner.* **32**, 504 (2005).
- [51] M. Akaogi, N. Horiuchi, T. Ishii, and H. Kojitani, *Phys. Chem. Miner.* **39**, 797 (2012).
- [52] A. Lavrentyev, B. Gabrelian, P. Shkumat, I. Nikiforov, T. Bondarenko, E. Kopylova, O. Khyzhun, M. Karpets, and J. Rehr, *J. Phys. Chem. Solids* **72**, 83 (2011).
- [53] J. Lukáč, M. Klementová, P. Bezdička, S. Bakardjieva, J. Šubrt, L. Szatmáry, and A. Grusková, *J. Mater. Sci.* **42**, 9421 (2007).
- [54] K. Cheng, K. Chhor, J.-P. Passarello, C. Colbeau-Justin, and A. Kanaev, *ChemistrySelect* **3**, 11118 (2018).
- [55] M. D. Hernández-Alonso, I. Tejedor-Tejedor, J. M. Coronado, J. Soria, and M. A. Anderson, *Thin Solid Films* **502**, 125 (2006).
- [56] A. Kitiyanan, S. Sakulkaemaruechai, Y. Suzuki, and S. Yoshikawa, *Compos. Sci. Technol.* **66**, 1259 (2006).
- [57] A. Naumenko, I. Gnatiuk, N. Smirnova, and A. Eremenko, *Thin Solid Films* **520**, 4541 (2012).
- [58] A. Jain, S. P. Ong, G. Hautier, W. Chen, W. D. Richards, S. Dacek, S. Cholia, D. Gunter, D. Skinner, G. Ceder, and K. a. Persson, *APL Mater.* **1**, 011002 (2013).
- [59] K. P. Singh, C.-H. Shin, H.-Y. Lee, F. Razmjooei, A. Sinhamahapatra, J. Kang, and J.-S. Yu, *ACS Appl. Nano Mater.* **3**, 3634 (2020).
- [60] V. Polliotto, E. Albanese, S. Livraghi, P. Indyka, Z. Sojka, G. Pacchioni, and E. Giamello, *J. Phys. Chem. C* **121**, 5487 (2017).
- [61] F. Gallino, C. D. Valentin, and G. Pacchioni, *Phys. Chem. Chem. Phys.* **13**, 17667 (2011).
- [62] M. Ismail, A. Hashmi, A. M. Rana, and S. Kim, *Nanotechnology* **31**, 325201 (2020).
- [63] R. Pérez-Hernández, D. Mendoza-Anaya, M. Fernández, and A. Gómez-Cortés, *J. Mol. Catal. A: Chem.* **281**, 200 (2008).
- [64] W. J. Mortier, S. K. Ghosh, and S. Shankar, *J. Am. Chem. Soc.* **108**, 4315 (1986).
- [65] I. Rivals and L. Personnaz, *Neurocomputing* **20**, 279 (1998).
- [66] R. E. Kalman, *Trans. ASME J. Basic Eng.* **82**, 35 (1960).
- [67] J. P. Perdew, K. Burke, and M. Ernzerhof, *Phys. Rev. Lett.* **77**, 3865 (1996).
- [68] P. Giannozzi, S. Baroni, N. Bonini, M. Calandra, R. Car, C. Cavazzoni, D. Ceresoli, G. L. Chiarotti, M. Cococcioni, I. Dabo, A. D. Corso, S. de Gironcoli, S. Fabris, G. Fratesi, R. Gebauer, U. Gerstmann, C. Gougoussis, A. Kokalj, M. Lazzeri, L. Martin-Samos, N. Marzari, F. Mauri, R. Mazzarello, S.

- Paolini, A. Pasquarello, L. Paulatto, C. Sbraccia, S. Scandolo, G. Scლაუzero, A. P. Seitsonen, A. Smogunov, P. Umari, and R. M. Wentzcovitch, *J. Phys.: Condens. Matter* **21**, 395502 (2009).
- [69] G. Prandini, A. Marrazzo, I. E. Castelli, N. Mounet, and N. Marzari, *npj Computational Materials* **4**, 72 (2018).
- [70] M. Amsler, S. Rostami, H. Tahmasbi, E. R. Khajepasha, S. Faraji, R. Rasoulkhani, and S. A. Ghasemi, *Comput. Phys. Commun.* **256**, 107415 (2020).
- [71] A. Togo and I. Tanaka, *Scr. Mater.* **108**, 1 (2015).
- [72] P. Tangney and S. Scandolo, *J. Chem. Phys.* **117**, 8898 (2002).
- [73] C. Pinilla, A. H. Irani, N. Seriani, and S. Scandolo, *J. Chem. Phys.* **136**, 114511 (2012).
- [74] See Supplemental Material at <http://link.aps.org/supplemental/10.1103/PhysRevMaterials.5.063605> for structural data of all clusters and ZrO₂ nanoparticles, and also the ANN potential parameters and weights discussed here.
- [75] I. Bandyopadhyay and C. M. Aikens, *J. Phys. Chem. A* **115**, 868 (2011).
- [76] D. Çakır and O. Gülseren, *J. Phys.: Condens. Matter* **24**, 305301 (2012).
- [77] M. Chen and D. A. Dixon, *Nanoscale* **9**, 7143 (2017).
- [78] S. Huygh, A. Bogaerts, A. C. van Duin, and E. C. Neyts, *Comput. Mater. Sci.* **95**, 579 (2014).
- [79] B. Kaewruksa, V. Vchirawongkwin, and V. Ruangpornvisuti, *J. Mol. Struct.* **1108**, 187 (2016).
- [80] S. Li and D. A. Dixon, *J. Phys. Chem. A* **114**, 2665 (2010).
- [81] S. M. Woodley, S. Hamad, J. A. Mejías, and C. R. A. Catlow, *J. Mater. Chem.* **16**, 1927 (2006).
- [82] S. M. Woodley, S. Hamad, and C. R. A. Catlow, *Phys. Chem. Chem. Phys.* **12**, 8454 (2010).
- [83] W. Zhang, Y. Han, S. Yao, and H. Sun, *Mater. Chem. Phys.* **130**, 196 (2011).
- [84] L. Zibordi-Besse, Y. Seminovski, I. Rosalino, D. Guedes-Sobrinho, and J. L. F. D. Silva, *J. Phys. Chem. C* **122**, 27702 (2018).
- [85] O. Lamiel-García, A. Cuko, M. Calatayud, F. Illas, and S. T. Bromley, *Nanoscale* **9**, 1049 (2017).
- [86] M. A. Rahman, S. Rout, J. P. Thomas, D. McGillivray, and K. T. Leung, *J. Am. Chem. Soc.* **138**, 11896 (2016).
- [87] M. Lazzeri, A. Vittadini, and A. Selloni, *Phys. Rev. B* **63**, 155409 (2001).
- [88] A. Christensen and E. A. Carter, *Phys. Rev. B* **58**, 8050 (1998).
- [89] M. V. Ganduglia-Pirovano, A. Hofmann, and J. Sauer, *Surf. Sci. Rep.* **62**, 219 (2007).
- [90] A. R. Puigdollers, F. Illas, and G. Pacchioni, *Rendiconti Lincei* **28**, 19 (2016).
- [91] A. R. Puigdollers, F. Illas, and G. Pacchioni, *J. Phys. Chem. C* **120**, 4392 (2016).
- [92] G. Pacchioni, *Eur. J. Inorg. Chem.* **2019**, 751 (2019).
- [93] F. Maleki and G. Pacchioni, *J. Phys. Chem. C* **123**, 21629 (2019).
- [94] E. Albanese, A. R. Puigdollers, and G. Pacchioni, *ACS Omega* **3**, 5301 (2018).
- [95] Á. Morales-García, R. Valero, and F. Illas, *Phys. Chem. Chem. Phys.* **20**, 18907 (2018).
- [96] Á. Morales-García, A. M. Escatllar, F. Illas, and S. T. Bromley, *Nanoscale* **11**, 9032 (2019).
- [97] O. Lamiel-García, K. C. Ko, J. Y. Lee, S. T. Bromley, and F. Illas, *J. Chem. Theory Comput.* **13**, 1785 (2017).